Properties of the ionized CGM and IGM: tests for galaxy formation models from the Sunyaev–Zel'dovich effect

S. H. Lim [ID],[1,2]★ D. Barnes [ID],[3] M. Vogelsberger [ID],[3] H. J. Mo,[1] D. Nelson [ID],[4] A. Pillepich [ID],[5] K. Dolag[6,7] and F. Marinacci [ID][8]

[1]*Department of Astronomy, University of Massachusetts, Amherst, MA 01003-9305, USA*
[2]*Department of Physics and Astronomy, University of British Columbia, 6224 Agricultural Road, Vancouver, BC V6T 1Z1, Canada*
[3]*Kavli Institute for Astrophysics and Space Research, Massachusetts Institute of Technology, Cambridge, MA 02139, USA*
[4]*Universität Heidelberg, Zentrum für Astronomie, Institut für theoretische Astrophysik, Albert-Ueberle-Str 2, D-69120 Heidelberg, Germany*
[5]*Max-Planck-Institut für Astronomie, Königstuhl 17, D-69117 Heidelberg, Germany*
[6]*Max-Planck-Institut für Astrophysik, Karl-Schwarzschild-Str 1, D-85748 Garching, Germany*
[7]*University Observatory Munich, Scheinerstraße 1, D-81679 Munich, Germany*
[8]*Department of Physics and Astronomy, University of Bologna, Via Gobetti 93/2, I-40129 Bologna, Italy*

ABSTRACT

We present a comparison of the physical properties of the ionized gas in the circumgalactic medium and intergalactic medium (IGM) at $z \sim 0$ between observations and four cosmological hydrodynamical simulations: Illustris, TNG300 of the IllustrisTNG project, EAGLE, and one of the Magneticum simulations. For the observational data, we use the gas properties that are inferred from cross-correlating the Sunyaev–Zel'dovich effect (SZE) from the *Planck* CMB maps with haloes and large-scale structure. Both the observational and simulation results indicate that the integrated gas pressure in haloes deviates from the self-similar case, showing that feedback impacts haloes with $M_{500} \sim 10^{12-13} \, \mathrm{M_\odot}$. The simulations predict that more than half the baryons are displaced from haloes, while the gas fraction inferred from our observational data roughly equals the cosmic baryon fraction throughout the $M_{500} \sim 10^{12-14.5} \, \mathrm{M_\odot}$ halo mass range. All simulations tested here predict that the mean gas temperature in haloes is about the virial temperature, while that inferred from the SZE is up to one order of magnitude lower than that from the simulations (and also from X-ray observations). While a remarkable agreement is found for the average properties of the IGM between the observation and some simulations, we show that their dependence on the large-scale tidal field can break the degeneracy between models that show similar predictions otherwise. Finally, we show that the gas pressure and the electron density profiles from simulations are not well described by a generalized NFW profile. Instead, we present a new model with a mass-dependent shape that fits the profiles accurately.

Key words: methods: statistical – galaxies: evolution – galaxies: formation – galaxies: haloes.

1 INTRODUCTION

The current understanding of galaxy formation is significantly limited due to the complexity of the physical processes responsible for the interchange of mass and energy between galaxies and their surroundings (e.g. Mo, van den Bosch & White 2010). Gas and dark matter fall into the potential wells of haloes, collapsed objects that form via gravitational instability from the initial matter fluctuations present in the early Universe. Gas is heated by the virial shock at the edge of dark matter haloes, but it eventually cools through radiation to form stars. Observations, however, have accumulated evidence for galactic-scale winds that can heat and return gas from galaxies to the circumgalactic medium (CGM; medium in the vicinity of dark matter haloes associated with galaxies) and intergalactic medium (IGM; diffuse medium between haloes), possibly driven

by the stellar and active galactic nucleus (AGN) feedback (e.g. Steidel et al. 2010; Jones, Stark & Ellis 2012; Martin et al. 2012; Newman et al. 2012; Rubin et al. 2014; Heckman et al. 2015; Chisholm et al. 2016; Tumlinson, Peeples & Werk 2017). The gas returned to the surrounding medium is mixed with gas newly accreted on to haloes from the cosmic web. It is still an open question whether the wind energy is large enough to return the gas from haloes to the IGM or whether a substantial portion of the gas recycles back on to galaxies (Stocke et al. 2013; Werk et al. 2014, 2016; Borthakur et al. 2016; Prochaska et al. 2017; Rudie et al. 2019). Clearly, a systematic investigation of the CGM and IGM properties will help us to improve our understanding of feedback.

With the advent of large CMB surveys, the Sunyaev–Zel'dovich effect (SZE; Sunyaev & Zeldovich 1972) provides a promising way to probe the CGM and IGM gas properties. The scattering of the CMB photons with the free electrons on their paths from the last scattering surface to the observer changes the CMB spectrum, which is called

★ E-mail: shlim1206@gmail.com

the SZE. The SZE produced by the thermal motions of electrons is referred to as the thermal SZE (tSZE), while that produced by the bulk motions of electrons is called the kinetic SZE (kSZE). Recent studies have demonstrated that the tSZE and kSZE from observations can be used to characterize the properties of the ionized gas in the CGM and IGM (Hand et al. 2012; Planck Collaboration XI 2013; Van Waerbeke, Hinshaw & Murray 2014; Hojjati et al. 2015; Ma et al. 2015; Hill et al. 2016, 2018; Lim et al. 2018a,b, 2020; de Graaff et al. 2019; Tanimura et al. 2019). Using the SZE to trace the gas has advantages that it can probe relatively low-density regions such as outskirts of haloes and the IGM compared to X-ray observations, and that the derived gas properties do not depend on the gas metallicity and ionization states unlike absorption line studies towards quasars.

Cosmological hydrodynamical simulations offer a theoretical framework to study the physical processes involved in galaxy evolution and the resulting properties of the CGM and IGM (e.g. Kereš et al. 2005, 2009; Faucher-Giguère, Kereš & Ma 2011a; Somerville et al. 2015; Oppenheimer 2018). Large simulations that trace the evolution of the matter in a box with a sidelength of hundreds of Mpc (e.g. Vogelsberger et al. 2013, 2014a; Crain et al. 2015; Schaye et al. 2015; Dolag, Komatsu & Sunyaev 2016; McCarthy et al. 2017; Pillepich et al. 2018b), and high-resolution 'zoom-in' simulations that focus on the evolution of individual haloes (e.g. Hopkins et al. 2014, 2018; Muratov et al. 2015; Fattahi et al. 2016; Sawala et al. 2016; van de Voort et al. 2016; Anglés-Alcázar et al. 2017; Grand et al. 2017; Hafen et al. 2019), incorporate the relevant physics to reproduce the properties of galaxies and gas from observations reasonably well (e.g. Faucher-Giguère et al. 2010, 2015, 2016; Faucher-Giguère & Kereš 2011b; Hummels et al. 2013; Nelson et al. 2018b). However, simulations that are known to reproduce a similar set of key observations have employed a wide range of physical models. In order to break the degeneracy between the models, we need to test the physical assumptions with more detailed observations. To this end, there have been studies that compared the properties of CGM and IGM between simulations and observations (Battaglia et al. 2012a; Biffi, Dolag & Böhringer 2013; Le Brun, McCarthy & Melin 2015; Schaye et al. 2015; Barnes et al. 2017; Gupta et al. 2017; McCarthy et al. 2017; Hill et al. 2018; Ayromlou et al. 2020). However, comparisons based on X-ray observations have been, in most cases, limited to haloes with $M_{500} \geq 10^{13-13.5}$ M$_\odot$ (e.g. Biffi et al. 2013; Schaye et al. 2015; Barnes et al. 2017; McCarthy et al. 2017) while feedback is expected to strongly impact haloes with $M_{500} \leq 10^{13-13.5}$ M$_\odot$ because of their shallow potential well (e.g. Le Brun et al. 2015; McCarthy et al. 2017; Ayromlou et al. 2020). A recent study by Truong et al. (2020) extended the comparisons to a lower mass but is restricted to a local volume out to ∼100 Mpc. Comparisons of the SZE spanning a wide range of mass down to group-size haloes have been limited to a few observational studies (e.g. Planck Collaboration XI 2013), which are known to be sensitive to methods used to derive the properties from observational data (Le Brun et al. 2015; Hill et al. 2018).

In this paper, we compare the observational inference based on the SZE from Lim et al. (2018a,b, 2020) with predictions from hydrodynamical simulations, providing comprehensive tests for galaxy formation models. The observational constraints we use have been obtained by employing a simultaneous matching of filtering to increase the signal-to-noise as well as to disentangle the projection effects of haloes along same line of sight (LOS), and found robust against systematic effects such as foreground/background fluctuations and beam smearing effect (Lim et al. 2020). We use the cross-correlations between the SZE signals, dark matter haloes, and large-scale environments as tests. The mass scale probed in our

analysis by haloes of $M_{500} = 10^{12-14.5}$ M$_\odot$ is where AGN feedback leaves the most evident signatures, hence a fertile regime for testing feedback models (although some models predict that feedback impacts a lower mass regime; see e.g. Ayromlou et al. 2020). In fact, we find that the impact of AGN feedback on the SZE, including whether it only increases the gas temperature or blows the gas to the outskirts of haloes or even out of haloes, depends highly on mass as well as implemented models.

This paper is organized as follows. We present the observational data and the simulations used for our analysis in Section 2. We present the comparisons between the observation and the simulations in Section 3. Finally, we summarize our findings and conclude in Section 4. Throughout the paper, we assume the *Planck* cosmology (Planck Collaboration XIII 2016) with $\sigma_8 = 0.816$, $h = 0.677$, $\Omega_m = 0.309$, and $\Omega_b = 0.0486$. We scale accordingly the results from observation or simulations that assumed other cosmologies. We define haloes based on R_{500}, a radius within which the mean density is 500 times the critical density, and on M_{500}, the mass enclosed within R_{500}. We note that, in this paper, we refer to the medium inside dark matter haloes as CGM while referring to the medium between haloes as IGM, and that our analysis is focused on the properties of their ionized component rather than their cold component.

2 DATA

2.1 The SZE

As the CMB photons pass through groups or clusters, they interact with free electrons therein via inverse Compton scattering due to thermal motion of the electrons (tSZE) or via Doppler effect due to bulk, kinetic motion of the electrons (kSZE), which results in a change in the energy spectrum of CMB.

The change of the CMB spectrum caused by the tSZE is characterized through a dimensionless parameter by[1]

$$\left(\frac{\Delta T}{T_{CMB}}\right)_{tSZE} = g(x)y \equiv g(x)\frac{\sigma_T}{m_e c^2} \int P_e dl, \tag{1}$$

where $T_{CMB} = 2.7255$ K, y is the Compton parameter, $g(x) = x \coth(x/2) - 4$ is the conversion factor at a given $x \equiv h\nu/(k_B T_{CMB})$, σ_T is the Thompson cross-section, m_e is the electron rest mass, c is the speed of light, $P_e = n_e k_B T_e$ is the electron pressure with n_e and T_e the number density and temperature, respectively, of the free electron, and finally dl is the path-length along the given LOS.

Similarly, the temperature change in the CMB spectrum by the kSZE is given by

$$\left(\frac{\Delta T}{T_{CMB}}\right)_{kSZE} = -\frac{\sigma_T}{c} \int n_e(\mathbf{v} \cdot \hat{\mathbf{r}}) dl, \tag{2}$$

where $\mathbf{v}$ is the velocity of the free electrons in bulk motion and $\hat{\mathbf{r}}$ is the unit vector along an LOS.

2.2 Observational constraints from the SZE

In this paper, we use the observational constraints obtained by Lim et al. (2018a,b, 2020). They are a series of papers that studied the gas properties in the CGM and IGM in a coherent way using

---

[1]In this paper, we ignore the relativistic corrections to the SZE, which is about 8 per cent for the tSZE for the most massive end of the mass range probed in our analysis, and then decreases proportionally with decreasing mass (Remazeilles et al. 2019; Lee et al. 2020).

the *Planck* observation (Tauber et al. 2010; Planck Collaboration I 2011) and a filtering approach to increase the signal-to-noise and properly account for the projection effects. Here, we only highlight their main findings and parts of their methods necessary for the analysis presented in this paper, and refer the reader to the original papers for the details regarding their methods, validation tests, and comparisons with other observations.

They used the group catalogues of Yang et al. (2005, 2007) and Lim et al. (2017), which contains a total of about half a million groups from 2MRS, 6dF, SDSS, and 2dF covering nearly the entire sky, combined with the reconstructed velocity field (Wang et al. 2012), to extract the average SZE flux associated with haloes of mass from 10^{12} to 10^{15} $M_\odot$. They generated model maps that include observational effects and projection effects, and minimized the χ^2 with respect to the *Planck* maps to constrain the models. To properly account for the beam smearing effect by the relatively large beam size of the *Planck* ranging between 5 and 31 arcmin, they applied filters mimicking the *Planck* beam to their model maps. They assumed the universal pressure profile (UPP) of Arnaud et al. (2010) for tSZE, and a β-profile constrained from South Pole Telescope clusters (Plagge et al. 2010) for kSZE, to determine the amplitudes of SZE signals and to convert the results to relevant integrated flux. They have shown that their results are robust against various noise sources and systematic effects including residual background/foreground fluctuations, beaming, residual dust emission, and uncertainty in the velocity reconstruction, as well as properly account for the projection effects. Additionally, they demonstrated that the results are also robust against truncation of the filters at different radii, mass incompleteness of the halo catalogue, moderate variations in the filter shape, and fluctuations of the background. They suspect that the results are insensitive to a moderate range of profiles because the beam size of the *Planck* does not resolve profiles for most of the targets. They found that the projection effects of larger haloes along LOSs, which are accounted for in their analysis, are significant for the signals from low-mass haloes. Using simulations, however, they also found that the method tends to overestimate the kSZE flux for low-mass haloes by up to 20 per cent, possibly because of the contamination by the projection of gas outside haloes along LOS. The projection effect is expected to depend on the baryonic processes such as the stellar and AGN feedback, with a higher projection effect from a stronger feedback.

The impact of feedback is believed not to be confined within haloes, but also leaves its imprint in the IGM. For a better understanding of feedback, it thus is helpful to investigate the SZE signal of the IGM. For this reason, we also include the IGM properties constrained by Lim et al. (2018b) for our comparison. They adopted a similar approach as described above, i.e. they constructed and filtered model maps, and compared with the *Planck* maps to constrain their models by minimizing the χ^2. They used the density field reconstructed on $1\,h^{-1}$Mpc scale for the Sloan Digital Sky Survey Data Release 7

(SDSS DR7; Abazajian et al. 2009) volume, by Wang et al. (2016). The reconstruction uses haloes identified by the group finder for the SDSS 7 region as a tracer of the underlying density field. Specifically, the SDSS volume is partitioned into domains associated with each halo. Then, the average profiles of haloes, calibrated from *N*-body simulations, are assumed to distribute the density field within each domain. Using simulation and mock catalogues, the method has been tested and found to be successful in reconstructing the density field. Thus, no significant bias in the reconstructed density field for the observational data (with respect to the density field simply calculated by summing up the particles in each cube of a $1\,h^{-1}$ Mpc side from simulations; see Section 3.3) is expected. Lim et al. (2018b) adopted and constrained a double power-law relation between the pressure and density of the IGM,

$$P_e = \begin{cases} A \times (\rho_m/\rho_{m,0})^{\alpha_1}, & \text{if } \rho_m \leq \rho_{m,0} \\ A \times (\rho_m/\rho_{m,0})^{\alpha_2}, & \text{if } \rho_m > \rho_{m,0}, \end{cases} \quad (3)$$

where $\rho_{m,0}$ is a characteristic density at which a transition in the slope is set to occur, and have found the median parameter values of $\{\rho_{m,0}/\overline{\rho}_m, \alpha_1, \alpha_2\} = \{3.0, 1.7, 2.2\}$. We refer the reader to L18b for more details of the posterior distribution of the parameters.

They also investigated the dependence of the pressure–density relation on the large-scale tidal field. This is motivated by findings based on simulations that, among various quantities such as stellar mass, star formation rate, black hole mass, velocity dispersion, etc., the large-scale tidal field is the most crucial second parameter that affects the gas pressure (Lim et al. 2018b). Following Wang et al. (2011), the halo-based tidal field for each grid cell of $(1\,h^{-1}\text{Mpc})^3$ is estimated as the halo tidal force exerted on the surface of a sphere along a direction $\boldsymbol{t}$, normalized by the self-gravity of the sphere:

$$f(\boldsymbol{t}) = \frac{\sum_i GM_i R_g (1 + 3\cos 2\theta_i)/r_i^3}{2GM_g/R_g^2}, \quad (4)$$

where the summation is over all the haloes, M_i is the mass of halo i, $R_g = 0.5\,h^{-1}$ Mpc is the radius of the sphere that approximates the grid cell, M_g is the mass enclosed within the grid cell in question, r_i is the separation between the centre of the grid cell and the halo 'i', and θ_i is the angle between $\boldsymbol{t}$ and $\boldsymbol{r}_i$. The tidal field satisfies $t_1 + t_2 + t_3 = 0$, where t_1, t_2, and t_3 $(t_1 \geq t_2 \geq t_3)$ are the eigenvalues of the tidal field tensor. Wang et al. (2011) showed that t_1 represents well the magnitude of the tidal field. We thus use t_1 to characterize the tidal field strength of the grid cells. For the computation of tidal field strengths from the observation, Lim et al. (2018b) used haloes identified in the group catalogue. As can be seen in equation (4), $f(\boldsymbol{t})$ and t_1 can be computed in the same manner for observation as is for simulations once haloes are identified. To test the uncertainty introduced by the halo identification, we constructed a mock survey of SDSS and applied the same halo finder as used by Lim et al. (2017, 2018b). From the test, we found no meaningful change in the resulting tidal field strength compared to the case that we use the true haloes directly identified in simulations. Throughout this paper, thus we use the observational data from Lim et al. (2018b) while for simulations we compute t_1 using the true haloes, ignoring the uncertainty of the halo finder.

2.3 Hydrodynamical simulations

For our analysis, we use a number of state-of-the-art cosmological gas simulations for galaxy evolution: Illustris, TNG300, Evolution and Assembly of GaLaxies and their Environments (EAGLE), and Magneticum (see below and Table 1 for details). These simulations

Table 1. List of the simulations used for comparisons. From left to right, the columns show simulation name, comoving box size, baryonic particle mass, and dark matter particle mass.

Simulation	L (h^{-1} Mpc)	m_{baryon} ($M_\odot$)	m_{DM} ($M_\odot$)
Illustris	75	1.6×10^6	6.3×10^6
TNG300	205	1.1×10^7	5.9×10^7
EAGLE	67.8	1.8×10^6	9.7×10^6
Magneticum	352	1.4×10^8	6.9×10^8

adopt different numerical techniques, cosmological models, and different implementations of physical processes, to trace the evolution of the simulated universe. All these simulations identify haloes using a friends-of-friends (FoF; Huchra & Geller 1982; Davis et al. 1985) algorithm.

2.3.1 Illustris

The first simulation is Illustris (Genel et al. 2014; Vogelsberger et al. 2014a,b; Sijacki et al. 2015), which was run with the moving-mesh code AREPO (Springel 2010), assuming a WMAP9 cosmology with $h = 0.704$, $\Omega_m = 0.273$, and $\Omega_\Lambda = 0.727$ (Hinshaw et al. 2013). The traced components include gas cells, dark matter particles, stars and stellar wind particles, and supermassive black holes. Sub-grid models are employed for the physical processes such as cooling (Katz, Weinberg & Hernquist 1996; Wiersma, Schaye & Smith 2009), star formation (Springel & Hernquist 2003) with a Chabrier (2003) initial mass function, stellar feedback (Vogelsberger et al. 2013; Torrey et al. 2014), and AGN feedback (Springel et al. 2005; Sijacki et al. 2007). For the detailed implementation, we refer the reader to Vogelsberger et al. (2013). The free parameters in the models were constrained using a set of mostly $z = 0$ observations of the galaxy populations. In this paper, we use Illustris-1, the fiducial run, that has a box size of $L = 75\,h^{-1}$ Mpc and contains $2 \times (1820)^3$ initial gas and dark matter particles. The target baryon mass and dark matter particle mass are $m_{baryon} = 1.6 \times 10^6$ M$_\odot$ and $m_{DM} = 6.3 \times 10^6$ M$_\odot$, respectively. The gravitational softening length for the dark matter particles is 1.4 kpc, and for the gas cells is adaptive with a minimum at about 0.7 ckpc.

2.3.2 TNG300

The IllustrisTNG project (Marinacci et al. 2018; Naiman et al. 2018; Nelson et al. 2018a; Pillepich et al. 2018b; Springel 2018), the successor of Illustris, is a series of hydrodynamical simulations run with the AREPO code including ideal magnetohydrodynamics (Pakmor et al. 2011) and assuming the cosmological model given by Planck Collaboration XIII (2016) with $\sigma_8 = 0.816$, $h = 0.677$, $\Omega_m = 0.309$, and $\Omega_b = 0.0486$. Here, we use the TNG300-1 run, the largest volume of the IllustrisTNG project (TNG300 hereafter), which is sampled with $(2500)^3$ dark matter particles and $(2500)^3$ initial gas cells in a periodic box of $(205\,h^{-1}$ Mpc$)^3$. The physical galaxy formation model of IllustrisTNG is an extension and improvement of the original Illustris model, and is detailed in the IllustrisTNG method papers (Weinberger et al. 2017; Pillepich et al. 2018a). One of the major changes in IllustrisTNG is a new model of black hole-driven kinetic feedback at low accretion rates (referred to as a wind mode), compared to the original Illustris where thermal energy from the feedback is injected into surrounding gas in a form of 'bubbles'. The target baryon mass and dark matter particle mass are $m_{baryon} = 1.1 \times 10^7$ M$_\odot$ and $m_{DM} = 5.9 \times 10^7$ M$_\odot$, respectively. The $z = 0$ Plummer equivalent gravitational softening of the collisionless component, and the minimum comoving value of the adaptive gas gravitational softening are 1.5 kpc and 0.37 ckpc, respectively.

2.3.3 EAGLE

The EAGLE (Crain et al. 2015; Schaye et al. 2015; McAlpine et al. 2016), run with a modified version of the GADGET-3 smoothed particle hydrodynamics code (Springel 2005), tracks the evolution of gas, stars, dark matter, and massive black holes in a simulated

universe, by implementing sub-grid models for cooling (Wiersma et al. 2009), star formation (Schaye & Dalla Vecchia 2008), and stellar and AGN feedbacks (Booth & Schaye 2009; Rosas-Guevara et al. 2016). The models are parametrized and the model parameters are tuned to match observations including the stellar mass function and stellar mass–black hole mass relation at $z \sim 0$. The simulation assumes the *Planck* cosmology (Planck Collaboration XVI 2014). For this paper, we use the simulation run of the largest box, $(100\,$Mpc$)^3$, sampled by $2 \times (1504)^3$ particles. The initial baryonic particle mass and dark matter particle mass are 1.8×10^6 M$_\odot$ and 9.7×10^6 M$_\odot$, respectively. The comoving Plummer-equivalent gravitational softening and the maximum physical softening length are roughly 2.7 kpc and 0.70 ckpc, respectively.

2.3.4 Magneticum

The Magneticum simulations (e.g. Dolag et al. 2016) are a set of cosmological hydrodynamical simulations with various volumes and resolutions, performed with an improved version of GADGET-3. The simulations adopted a WMAP7 flat ΛCDM cosmology with $\sigma_8 = 0.809$, $h = 0.704$, $\Omega_m = 0.272$, and $\Omega_b = 0.0456$ (Komatsu et al. 2011). The simulations include a variety of physical processes such as cooling and star formation (Springel & Hernquist 2003), black holes and AGN feedback (Fabjan et al. 2010; Hirschmann et al. 2014), and thermal conduction (Dolag et al. 2004). The results presented in this paper are produced from a particular run that has a box size of $L = 352\,h^{-1}$ Mpc and is sampled by $2 \times (1584)^3$ particles. The dark matter particle mass and gas particle mass are 6.9×10^8 M$_\odot$ and 1.4×10^8 M$_\odot$, respectively. The softening lengths are 3.8 kpc commonly for dark matter and gas particles.

3 RESULTS

3.1 The thermal energy of halo gas

Assuming a UPP shape with amplitudes determined from χ^2 minimization, Lim et al. (2018a, hereafter L18a) inferred from observational data the integrated tSZE flux within R_{500}, Y_{500}, defined by

$$d_A(z)^2 Y_{500} \equiv \frac{\sigma_T}{m_e c^2} \int_{R_{500}} P_e \, dV, \qquad (5)$$

where $d_A(z)$ is the angular diameter distance to a halo at given redshift. At a fixed halo mass, Y_{500} evolves with redshift as $E^{2/3}(z)$. Thus, it is conventional to define a redshift-independent quantity scaled to $z = 0$:

$$\tilde{Y}_{500} \equiv Y_{500} E^{-2/3}(z) \left(\frac{d_A(z)}{500\,\text{Mpc}} \right)^2, \qquad (6)$$

which is expected to be a function of only halo mass if the intrinsic tSZE flux follows a self-similar expectation across redshifts, i.e. the expectation from the virialization and a fixed baryon fraction at a given mass. The $\tilde{Y}_{500}$ thus inferred from the medians and 68 percentile ranges of the posterior distribution of the model parameters from L18a are shown by the yellow triangles and the error bars, respectively, in Fig. 1.

The dashed line shows the self-similar case of Arnaud et al. (2010), obtained from a combination of X-ray observations and simulations, that here we show extrapolated to a much lower mass than that probed in the original paper. The curve for the self-similar case in the extrapolated regime is shown in light grey while that in the mass scale directly probed in the original paper is in dark grey. We also
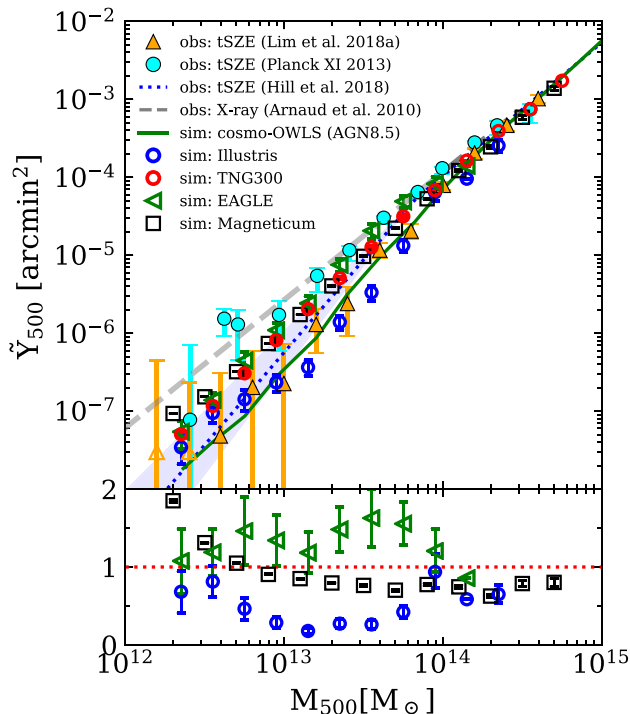
Figure 1. Comparison of the tSZE flux from gas within R_{500} of haloes, $\tilde{Y}_{500}$, between several observations [Lim et al. (2018a, up-pointing triangles), Planck Collaboration XI (2013, cyan dots), Hill et al. (2018, dotted), and Arnaud et al. (2010, dashed)] and simulations [cosmo-OWLS (Le Brun et al. 2015, green solid), Illustris (blue dots), TNG300 (red dots), EAGLE (left-pointing triangles), and Magneticum (squares)]. For the yellow triangles, the error bars represent the 68 percentile ranges of the posterior distribution, and the unfilled symbols are used to indicate negative values. The error bars for the simulations indicate the 68 percentile ranges of the mean obtained from 10 000 bootstrap samples. In the lower panel, we show the ratio of the predictions from the simulations to that from TNG300.

present results from other observational studies, including Planck Collaboration XI (2013, hereafter PCXI; cyan dots) and Hill et al. (2018, blue dotted line). In order to account for different cosmologies assumed in the studies, we scale the results to the *Planck* cosmology with respect to the self-similar case, $\int_{R_{500}} P_e \, dV \propto (\Omega_b / \Omega_m) \, h^{2/3}$. Using the *Planck* temperature maps, and locally brightest galaxies as a tracer of haloes, PCXI found that the tSZE flux follows the self-similar case, i.e. the thermal energy of hot gas relative to that of virialized haloes is independent of halo mass, whereas L18a reported a significantly lower thermal energy in lower mass systems. L18a suspect that the discrepancy arises because PCXI did not fully take into account the projection effects of other haloes. PCXI tested both aperture photometry and matched filter to extract the flux, but in both cases they assumed flat local backgrounds to subtract. As demonstrated in Vikram, Lidz & Jain (2017), however, the two-halo terms dominate the tSZE signals around haloes of $M_{200} \leq 10^{13-13.5} \, h^{-1} \mathrm{M}_{\odot}$; thus, even a very small deviation from flat backgrounds can significantly change the estimation of the tSZE flux for those haloes. L18a confirmed that they recover the PCXI results when assuming flat backgrounds, implying that local background indeed changes with distance from halo centres due to the clustering of haloes. Taking into account the projection effects based on Vikram et al. (2017), Hill et al. (2018) also found some evidence for a deviation of the relation from the self-similar case. As seen in Fig. 1, their results are consistent with the results from L18a even down

to low-mass systems. Hill et al. used the *Planck* map and the halo catalogue by Yang et al. (2007), which is very similar to the data set that L18a used.

Fig. 1 compares the observational results with the predictions from the simulations described in the previous section. To compute $\tilde{Y}_{500}$ from the simulations, we sum up the thermal energy of all ionized gas particles/cells that are associated with each simulated halo by the FoF algorithm and that are within a three-dimensional sphere of a radius R_{500}, without any temperature cut. The constants are multiplied according to equations (5) and (6). Note that $\tilde{Y}_{500}$ values from the simulations obtained this way do not contain any two-halo contribution or projection effects. The measurements from the simulations with different cosmologies are corrected to the *Planck* cosmology in the same way as was done for the observations. The error bars are obtained from 10 000 bootstrap samples. It is clearly seen that all simulations considered in our analysis predict a certain degree of deviation from the self-similar case, as is seen in the case for the L18a observational constraints (see also Battaglia et al. 2012a). The tSZE flux predicted by EAGLE and TNG300 are marginally consistent with that from L18a and Hill et al. (2018), within the uncertainties, which are typically up to a factor of 2–3. Magneticum predicts higher tSZE flux for haloes with $M_{500} \leq 10^{12.5} \, \mathrm{M}_{\odot}$ than EAGLE and TNG300. On the other hand, Illustris, which implements a somewhat more violent AGN feedback than the other simulations (see Genel et al. 2015; Pillepich et al. 2018a,b), predicts a much lower electron pressure than the other simulations, and more than an order of magnitude lower pressure than the self-similar case for haloes with $M_{500} \sim 10^{13-13.5} \, \mathrm{M}_{\odot}$. Those haloes are the systems that are believed to be strongly affected by the AGN feedback, suggesting that the discrepancies in the tSZE flux are due to the differing implementations of AGN feedback.

3.2 The mass and temperature of halo gas

Using the amplitudes of the β-profile determined as described in Section 2.2, Lim et al. (2020, hereafter L20) inferred from observational data the total hot gas mass within R_{500} as

$$M_{\mathrm{gas}} = N_{\mathrm{e},500} \cdot \frac{2m_p}{1 + f_H}, \qquad (7)$$

where $N_{\mathrm{e},500} = \int_{R_{500}} n_e \, dV$, $f_H = 0.76$ is the hydrogen mass fraction, and m_p is the proton mass. Fig. 2 shows the averages (the yellow circles) and the dispersions (the error bars) of the gas mass fraction from the seven observational samples described in L20. The shaded band spans the dispersion among the seven samples, inferred from a power-law model (see L20 for details). As seen in the figure, the inferred gas fraction is consistent with the cosmic baryon fraction (black dashed); thus, there is no missing baryon in haloes. This is consistent with findings of Hernández-Monteagudo et al. (2015) that reported the detection of all baryons on halo scale from cross-correlation of SDSS galaxies with the kSZE of the *Planck* data. However, it is at odds with standard X-ray analyses, particularly for haloes below $\lesssim 10^{14} \mathrm{M}_{\odot}$ – see below.

We compare the gas fraction from the kSZE with that inferred from the tSZE results by assuming that the gas is at the virial temperature, $T_{\mathrm{vir}} = \mu m_p G M_{500} / 2 k_B R_{500}$ (where $\mu = 0.59$ is the mean molecular weight), which is shown by the magenta dot–dashed line with the band showing the errors in the estimate. The inferred gas fraction from the tSZE is significantly lower particularly in low-mass systems than that from the kSZE. This implies that the effective temperature of the gas is much lower than the virial temperature as discussed in L20.
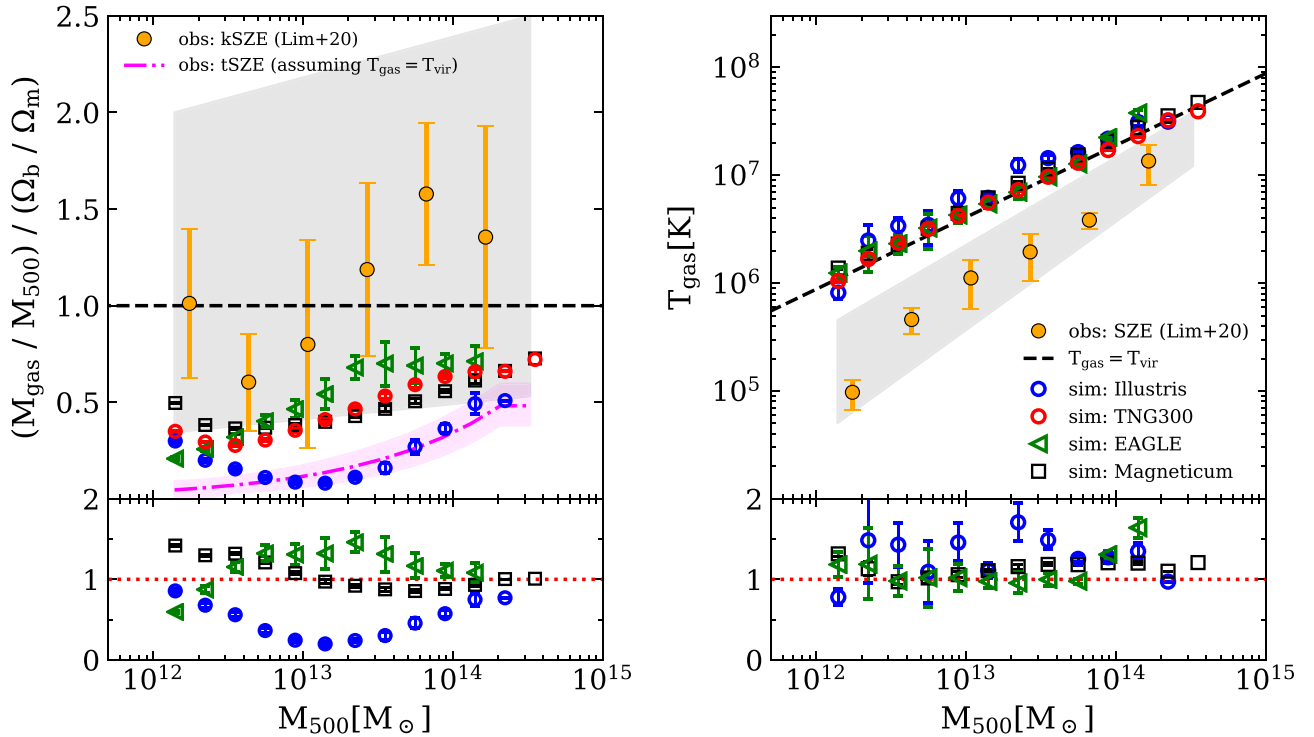
Figure 2. Halo gas mass (left) and effective temperature (right) in comparison to the SZE-inferred observational constraints from Lim et al. (2020, filled circle). The temperatures from the simulations are calculated as $T_{\mathrm{eff}} = \int_{R_{500}} n_e T_e \, \mathrm{d}V / \int_{R_{500}} n_e \, \mathrm{d}V$. The error bars for the observational result represent the dispersion of the estimate among the seven samples as described in Lim et al. (2020). The shaded band spans the same dispersion among the seven samples but obtained with a power-law model from Lim et al. (2020). The error bars for the simulations indicate the 68 percentile ranges of the mean obtained from 10 000 bootstrap samples. The dashed line shows the cosmic baryon fraction and the virial temperature $T_{\mathrm{vir}} = \mu m_p G M_{500} / 2 k_B R_{500}$ in the left- and right-hand panels, respectively. In the left-hand panel, the dot–dashed curve indicates the gas mass fraction inferred from the tSZE analysis by assuming $T_{\mathrm{gas}} = T_{\mathrm{vir}}$, with the band showing the uncertainty. In the lower panels, we show the ratio of the predictions from the simulations to those from TNG300.

We compare the observationally kSZE-inferred gas fractions with the predictions from the simulations. The latter is calculated in the simulations by summing up the ionized mass of all gas particles/cells within a three-dimensional sphere of R_{500} that are associated with each simulated halo in question through the FoF, and dividing it by total halo mass and the cosmic baryon fraction. The error bars for the simulations are obtained from 10 000 bootstrap samples. Overall, the simulations predict lower gas fractions than the observational results across the whole mass range considered here, up to by a factor of ~ 4 at the low-mass end of $M_{500} \sim 10^{12}$ M$_\odot$. This also means that the simulations predict 20–40 per cent lower baryons in low-mass systems relative to the cosmic fraction. Illustris has a much higher fraction of gas expelled out of the halo potential than the other simulations, possibly due to the stronger AGN feedback implemented (Genel et al. 2014; Pillepich et al. 2018a).

We also present the effective temperature, T_{eff}, from L20 obtained by dividing the total tSZE flux with the total kSZE flux, in the right-hand panel of Fig. 2. The inferred temperature (and also the inferred baryon fraction as they are connected to each other through the tSZE measurement) is in conflict with that reported from X-ray observations as pointed out and discussed in detail by L20. The temperature (baryon fraction) is found to be significantly lower (higher) than that from X-ray observations (e.g. Vikhlinin et al. 2006; Giodini et al. 2009; Sun et al. 2009; Gonzalez et al. 2013; Lovisari, Reiprich & Schellenberger 2015). As discussed in L20, this may be due to the difference between the mass-weighted temperature and X-ray temperature, the latter of which weighs more in the inner

dense, hotter region. Simulations found that the X-ray temperature is indeed higher than the mass-weighted temperature (e.g. Nagai, Vikhlinin & Kravtsov 2007a; Truong et al. 2020). The mass derived from X-ray also tends to be lower than the true halo mass by 0.2–0.3 dex on average (Nagai et al. 2007a), which results in a further bias to a higher temperature at a given mass. The net bias for the temperature comparison, however, is unclear since it depends on the gas distribution and properties that are not well understood in detail and largely model dependent. The discrepancy, however, may be real and indicate that the gas responsible for the SZE and X-ray emission cannot be described well by a single component, but is composed of multiple components in different phases. Wu et al. (2020) found that both the SZE and X-ray data can be accommodated well simultaneously by a two-phase model where two gas components at different temperatures are assumed. They have shown that, in their model, the hot component is still found to be about at the virial temperature and comprises 20–60 per cent in mass, while the total ('hot' + 'warm' components) gas mass fraction is close to the cosmic baryon fraction. The finding by Wu et al. (2020) thus indicates that the apparent discrepancy between the temperature inferred from the SZE and X-ray is not a conflict, but a reflection of multiphases of the gas components, and arises from different weightings by the two observations of temperatures of the multiple components.

Yet another uncertainty included in the comparison of the temperature is that of the group catalogue used. While the group catalogue adopted in L18a and L20 has been confirmed to yield unbiased halo mass estimate, it has a typical scatter of 0.2–0.3 dex in mass

estimate. In a forthcoming paper (Lim et al., in preparation), the impact of the scatter in mass will be further studied in detail. Another source of uncertainty is the offset of the halo centres identified by the halo finder relative to the true centre. The miscentring will result in an underestimation of both the tSZE and kSZE signals. This will result in an underestimation of the temperature because the tSZE profile is expected to decrease more rapidly as going away from the halo centres than the kSZE profile. Furthermore, due to the nature of the simultaneous matching, the results for different mass bins are correlated, with a slight under(over)estimation for massive haloes possibly leading to a significant over(under)estimation for lower mass haloes (see L20). Finally, if the assumed profiles are not good approximations of true underlying profiles, that may introduce additional bias in the integrated fluxes. We investigate all these potential systematics in detail in a forthcoming paper (Lim et al., in preparation) where preliminary results show that all the systematics change the results within the 1σ uncertainty.

For comparison, we estimate the effective temperature, $T_{\text{eff}} = \frac{\int_{R_{500}} n_e T_e \, dV}{\int_{R_{500}} n_e \, dV}$, from the simulations. The results are scaled with respect to the virial temperature, $T_{\text{vir}} \propto h^{2/3}$, to correct for the different cosmologies adopted in the simulations. As seen in Fig. 2, right-hand panel, all the simulations predict that the effective temperature of the gas is about the virial temperature, which is up to an order of magnitude higher than that inferred from the SZE analysis. It is interesting to note that the simulations with a wide range of feedback models predict very similar temperature of gas in haloes. Indeed, Fig. 2 shows that the difference between the gas fractions predicted from the simulations is more significant than that in between the temperatures. In particular, EAGLE provides a simulation run for a smaller box (of a sidelength of 50 Mpc) with the 'AGNdT9' model, where the AGN is set to heat the gas to a higher temperature of 10^9 K; thus, the feedback is more energetic and effective than in their fiducial model while the other parts of the simulation are kept the same. We directly confirm that their 'AGNdT9' model predicts a much lower gas fraction at any given mass (typically by more than a factor of 2) but predicts nearly the same temperature, relative to their fiducial model (see also Barnes et al. 2017). All this indicates that the variations in the feedback models implemented in the simulations do not affect much the prediction about the temperature of halo gas, while they change the effectiveness at ejecting gas out of haloes significantly. This also indicates, in parallel, that the discrepancy between the simulation predictions and the SZE data shown here may be due to other factors in the numerical simulations than the models implemented for feedback, such as modelling multiphase gas components.

3.3 The pressure–density relation of IGM

Fig. 3 shows the pressure–density relation obtained by Lim et al. (2018b, hereafter L18b) with the power-law model as described in Section 2.2, by the red solid line with the band showing the 1σ scatter based on the posterior distribution. As one can see from the median values of the parameters, the relation closely follows that of an adiabatic equation of state, $P_e \sim \rho^{5/3}$, but with a steeper slope in dense regions. The steeper slope may indicate an extra amount of heating sources available in dense regions due to feedback arising from star formation.

In the figure, we also compare the observational result with the predictions from the simulations. The predictions are calculated by summing up the mass and thermal energy of particles within each grid cell of $(1 \, h^{-1} \text{Mpc})^3$ from the simulations and dividing them by
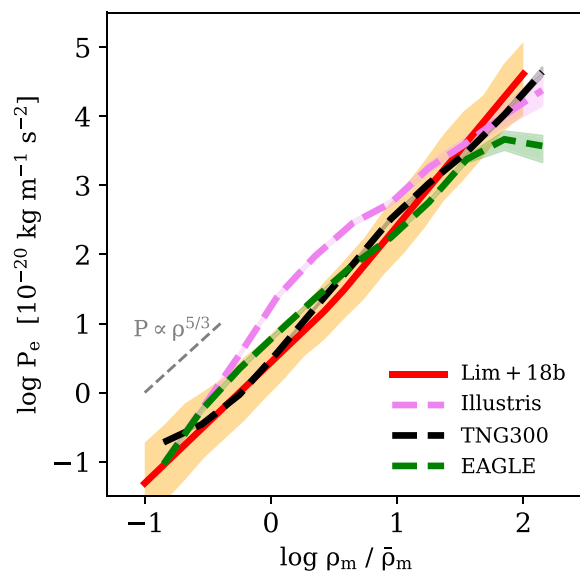

Figure 3. The pressure–density relation of IGM gas, compared with that from the simulations. The red line shows the mean relation obtained with our method, with the orange band showing the 1σ dispersion estimated from the uncertainties in the constrained parameters. The violet, black, and green lines show the mean relation from Illustris, TNG300, and EAGLE, respectively, with the bands indicating the 68 percentile ranges of the mean from 10 000 bootstrap samples.

the volume of the grid cells. Then, the average over all grid cells and its uncertainty are taken using 10 000 bootstrap samples. As one can see, the agreement of the observational result with TNG300 and EAGLE is remarkable. Compared to TNG300, EAGLE predicts a higher thermal energy (up to a factor of 3) in the underdense regions of $0.3 \leq \rho_m/\overline{\rho}_m \leq 1$, while it predicts a lower thermal energy in the regions of $10 \leq \rho_m/\overline{\rho}_m$, which are the regions corresponding to the cosmic structures. Illustris predicts a much higher thermal energy in the regions with $1 \leq \rho_m/\overline{\rho}_m \leq 10$, again, possibly due to the stronger radio-mode AGN feedback implemented in the simulation. One can convert the relations on to the temperature–density space, by assuming that each of the grid cells has the average ionized gas mass fraction equal to the cosmic baryon fraction, as is confirmed to be the case from simulations (see L18b). The temperature thus estimated is lower than 10^4 K in the regions with $\rho_m \leq \overline{\rho}_m$, and increases with the density, up to 10^6 K in the regions with $\rho_m \geq 100 \overline{\rho}_m$, which correspond to haloes.

L18b also sub-sampled the grid cells into three according to their tidal field strength, t_1, with each sub-sample containing a third of the total number of cells at a given density, and constrained the pressure–density relation for the three sub-samples jointly. We do the same calculation for the simulations for comparison by computing t_1 for the grid cells in the simulations as described in Section 2.2, and by dividing the cells into three equal-sized sub-samples according to their ranking in t_1. The average relations between the pressure and matter density thus estimated from the observation and the simulations are shown in Fig. 4. Both the simulations and the observation result show that the thermal energy of IGM at a given mass density is higher in the regions with the stronger tidal field. This may be due to that the regions with stronger tidal field are within or near massive structures, which cause the strong tidal field, where stronger stellar and AGN feedbacks are produced, resulting in more supply of heating. The tidal field dependence predicted by Illustris is much stronger than that from the observation as well
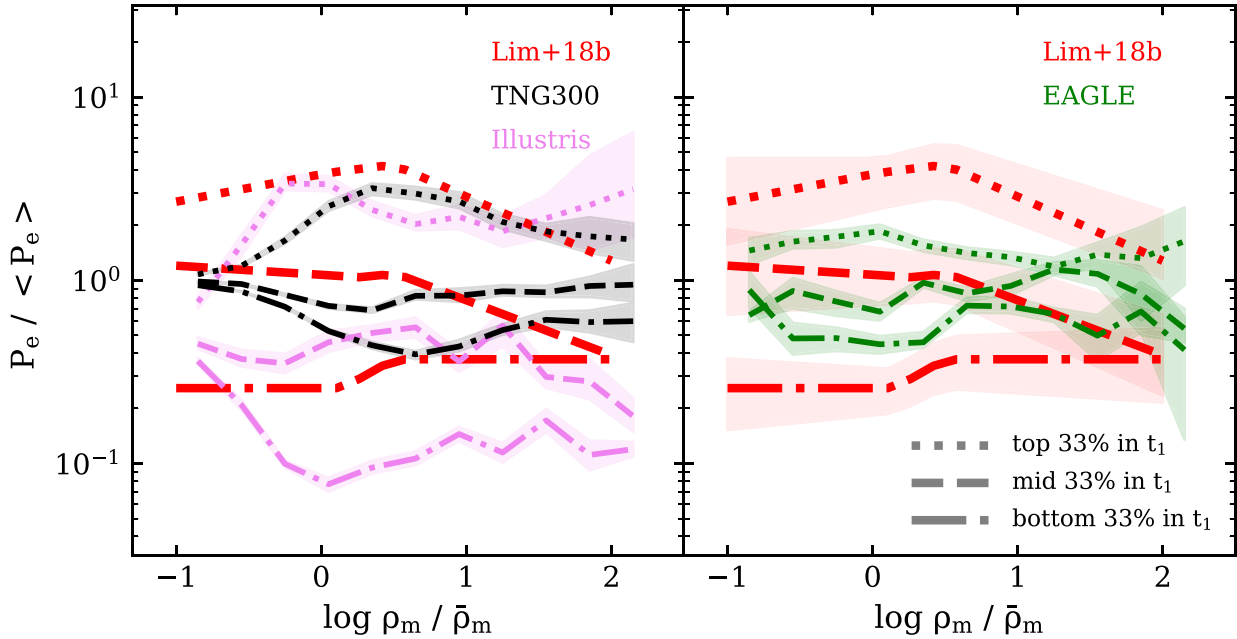
Figure 4. The pressure–density relation obtained for the three sub-samples of the grid cells according to their ranking in the tidal field strength, t_1, at given density. The red lines show the mean relations obtained from the observational data, with the shaded bands indicating the 1σ dispersions estimated from the posterior distribution of the model parameters. The dispersions are presented only in the right-hand panel, while they are same for the left-hand panel, for visual clarity. The results are compared with the predictions from TNG300 and Illustris (left-hand panel) and EAGLE (right-hand panel). The shaded regions for the simulations indicate the 68 percentile ranges of the mean obtained from 10 000 bootstrap samples. For each case, the results are normalized by the mean relation from the whole sample of the grid cells shown in Fig. 3.

as from the other simulations, which reflects the stronger AGN feedback implemented in Illustris. One can see that the prediction about the tidal field dependence distinguishes TNG300 and EAGLE with a much greater difference of up to 4σ–5σ [particularly at $(1$–$10)\,\overline{\rho}_m$], compared to the similarities shown mostly within 1σ–1.5σ for the other predictions such as the gas contents of haloes and the total average pressure of IGM. TNG300 predicts much stronger dependence on the tidal field strength than EAGLE for the regions with $(1$–$10)\,\overline{\rho}_m$, which correspond to cosmic filaments and sheets, and weaker dependence in underdense regions. This may be due to that TNG300, unlike EAGLE, implemented two different models for two modes of the AGN feedback. Specifically, TNG300 employed a kinetic feedback model for the AGN at low accretion rates while a thermal feedback model, as previously implemented in Illustris, was adopted for high accretion rates. Oppenheimer et al. (2020) showed that, due to the two different modes of feedback, predictions for haloes at a given mass from TNG300 present highly bimodal distributions relative to EAGLE, which uses a single model for the AGN feedback. The much stronger dependence on the tidal field shown here also can be because the kinetic 'wind-mode' feedback, which is far more efficient at ejecting halo gas than the thermal model (Weinberger et al. 2017), is more active in the region of a stronger tidal field. This gives an interesting hint that refining the balance between the modes and their strengths may improve the simulations towards more realistic models. Specifically, this could be explored by tuning the model parameters of feedback mode that is the main mechanism in the underdense regions, to increase the feedback efficiency.

Although simulations are consistent with the observation in that the thermal energy of gas is higher in the regions of the stronger tidal field, they fail to match the observation in detail. Compared to observation, EAGLE predicts much weaker dependence on the tidal

field in the density regimes corresponding to cosmic structures, while both TNG300 and EAGLE predict significantly weaker dependence in underdense regions. All these clearly demonstrate the potential of leveraging cross-correlations with secondary parameters such as environment rather than just with haloes or galaxy systems, for providing stringent tests on galaxy models and thus for breaking degeneracies between them.

3.4 The profiles of halo gas properties

We also investigate the profiles of gas properties including the pressure, temperature, and number density of free electrons, in proximity of galaxy haloes from the simulations. For the calculation of the profiles, we take into account all free electrons in each radial bin regardless of whether such electrons are associated with a halo in question or not. We find that accounting only for particles associated with haloes lowers the pressure and density profiles typically by less than 10 per cent (50 per cent) at $1.5R_{500}$ ($2R_{500}$). The pressure and density profiles are calculated by integrating the thermal energy and mass of free electrons, respectively, associated with gas particles/cells within each radial bin and by dividing them with the volumes enclosed in the corresponding shells. For the temperature profile, we calculate the effective temperature, $T_{\mathrm{eff}}(r) = \frac{\int_{\Delta r} n_e T_e \, dV}{\int_{\Delta r} n_e \, dV}$, i.e. in the same way as can be obtained by combining the tSZE and kSZE from observation. The average profiles are shown in Fig. 5 for selected halo mass bins, with the bands showing the errors in the means obtained from 10 000 bootstrap samples. The results are corrected to the *Planck* cosmology with respect to the virial temperature and universal baryon fraction.

For massive haloes, Illustris predicts shallower profiles for the pressure and temperature compared to the other simulations, with less gas near the halo centre, implying that the stronger AGN feedback
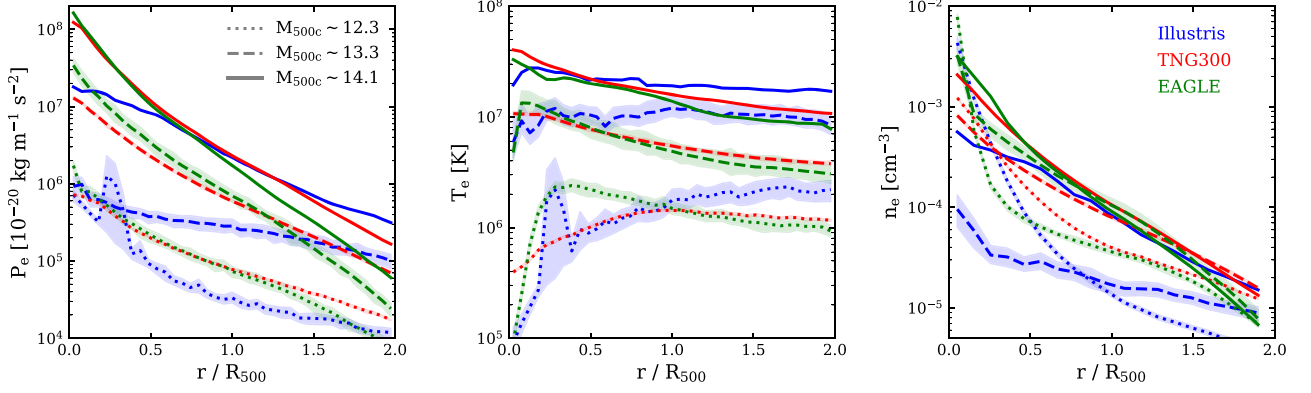
Figure 5. Comparison of the pressure (left), effective temperature (middle), and electron number density (right) profiles of gas associated with haloes of different masses between the simulations. Different line styles were used for the profiles in haloes of different masses as indicated. The shaded regions for the simulations indicate the 68 percentile ranges of the mean obtained from 10 000 bootstrap samples.

implemented in Illustris removes the gas from halo centre to the outskirts. That also explains the higher temperature in the outer region of haloes from Illustris. TNG300 also shows slightly shallower profiles than EAGLE, possibly due to the stronger 'wind-mode' AGN feedback that pushes the gas to the outer region of haloes more effectively than the thermal feedback model implemented in EAGLE.

For intermediate-mass haloes, the same trends as seen for the massive haloes continue but are much more strengthened. Illustris predicts more than an order of magnitude lower density in the inner region, and much less smooth temperature profile. For low-mass haloes, the difference among the simulations at $r \leq 0.5R_{500}$ is weaker than that for intermediate-mass haloes, indicating that haloes strongly affected by different galaxy formation models are those with a mass around 10^{13} M$_\odot$. It is interesting to note that, in Illustris, the gas in the outskirts of haloes is much less dense but is at a higher temperature than that in TNG300 and EAGLE, implying that feedback implemented in Illustris expels gas completely out of low-mass haloes rather than just to outer regions that are still in proximity of the haloes. The temperature of the gas from Illustris is found to be much more stochastic compared to the other two simulations.

The functional form of the UPP is a generalized NFW (GNFW) model (Nagai, Kravtsov & Vikhlinin 2007b), given by

$$\frac{P_e(r)}{P_{e,0}} = \frac{1}{(c_{500}\, r/R_{500})^\gamma [1 + (c_{500}\, r/R_{500})^\alpha]^{(\beta-\gamma)/\alpha}}, \quad (8)$$

where $P_{e,0}$ is a normalization parameter, and the parameters γ, α, and β describe the slopes at $r \ll r_s$, at $r \sim r_s$, and at $r \gg r_s$, respectively, with $r_s = R_{500}/c_{500}$. It was shown that the pressure profile of X-ray groups and clusters from observations is well described by the GNFW model (e.g. Arnaud et al. 2010; Plagge et al. 2010) but X-ray only allows to probe out to $r \sim R_{500}$ in most cases. Using a combination of X-ray observation and simulations, Arnaud et al. (2010) found the best parameter values of $\{\alpha, \beta, \gamma, c_{500}\} = \{1.05, 5.49, 0.308, 1.18\}$.

Le Brun et al. (2015) (LB15 hereafter) found that the pressure distribution predicted from simulations is not well described by the GNFW for haloes of different masses, but requires an additional parameter for a mass dependence of c_{500} instead,

$$c_{500} = c_{500,0}\, (M_{500}/10^{14}\mathrm{M}_\odot)^\delta. \quad (9)$$

As seen in the equation, this extended GNFW (EGNFW, hereafter) suggests that the concentration parameter may be a function of mass, which is a reasonable expectation given potentially different impacts

of feedback on haloes of different mass. LB15 indeed found a non-zero mass dependence with $\delta \sim 0.273$, indicating that the gas pressure is more concentrated in massive haloes than in lower mass haloes. This may be because the gas at the centre is blown out to the outskirts by galactic feedback more effectively in lower mass haloes, resulting in a shallower profile.

Here, we find, however, that the profiles measured from TNG300, Illustris, and EAGLE are not described well even by the particular form of EGNFW used in LB15. This is because the asymptotic slope of the profiles in the innermost region, described by γ in equation (8), is not universal for haloes of different masses, as clearly seen in Fig. 5. This means that an additional parameter describing a mass dependence in γ is required.

To this end, we suggest another form of the EGNFW model to describe the profiles:

$$P_e(r), n_e(r) \propto \frac{1}{(c_{500}\, r/R_{500})^\gamma [1 + (c_{500}\, r/R_{500})^2]^{(\beta-\gamma)/2}}, \quad (10)$$

where

$$\gamma = \gamma_0\, (M_{500}/10^{14}\, \mathrm{M}_\odot)^\epsilon, \quad (11)$$

with the concentration parameter following the same parametrization as in equation (9). Though the functional form is slightly different, this is conceptually very similar to the constrained fit dependent on mass in Battaglia et al. (2012b) and to the e-GNFW profile adopted in Gupta et al. (2017) to fit the pressure profiles from Magneticum, who found that the fit is greatly improved relative to fitting with the GNFW profile. Unlike the GNFW or LB15, we here choose to fix α because we find a significant degeneracy between α and c_{500} when both parameters are free. This is as expected because, from equation (8), α determines the profile slope at $r \sim r_s$ while c_{500} is directly related to r_s. The value of $\alpha = 2$ was chosen to be very close to the value found by LB15 (see Table 2).

We fit the pressure profiles measured from the simulations with the GNFW and our new EGNFW model, which are shown by the dashed and solid lines, respectively, in the upper panels of Fig. 6. The best-fitting parameters for the EGNFW model are listed in Table 2. Unlike LB15, the normalization of the profile, $P_{e,0}$, is treated as a free parameter in our model, the value of which is independently determined for haloes of different masses. We choose to do so because our main interest is the shape of profiles rather their amplitudes. It is clearly seen that the GNFW model, in which a profile shape is independent of mass, is insufficient to describe

Table 2. The best-fitting parameters of the EGNFW model for the pressure profiles, in comparison with other models from literature.

Profiles	α	β	γ_0	ϵ	$c_{500,0}$	δ
Illustris	2 (fixed)	3.76	0.0545	-0.803	1.20	0.517
TNG300	2 (fixed)	4.01	0.456	-0.0460	1.67	0.213
EAGLE	2 (fixed)	6.82	0.708	0.0338	1.02	0.129
Arnaud et al. (2010)	1.05	5.49	0.308	0 (fixed)	1.18	0 (fixed)
Le Brun et al. (2015)	2.02	3.84	1.08	0 (fixed)	1.04	0.273
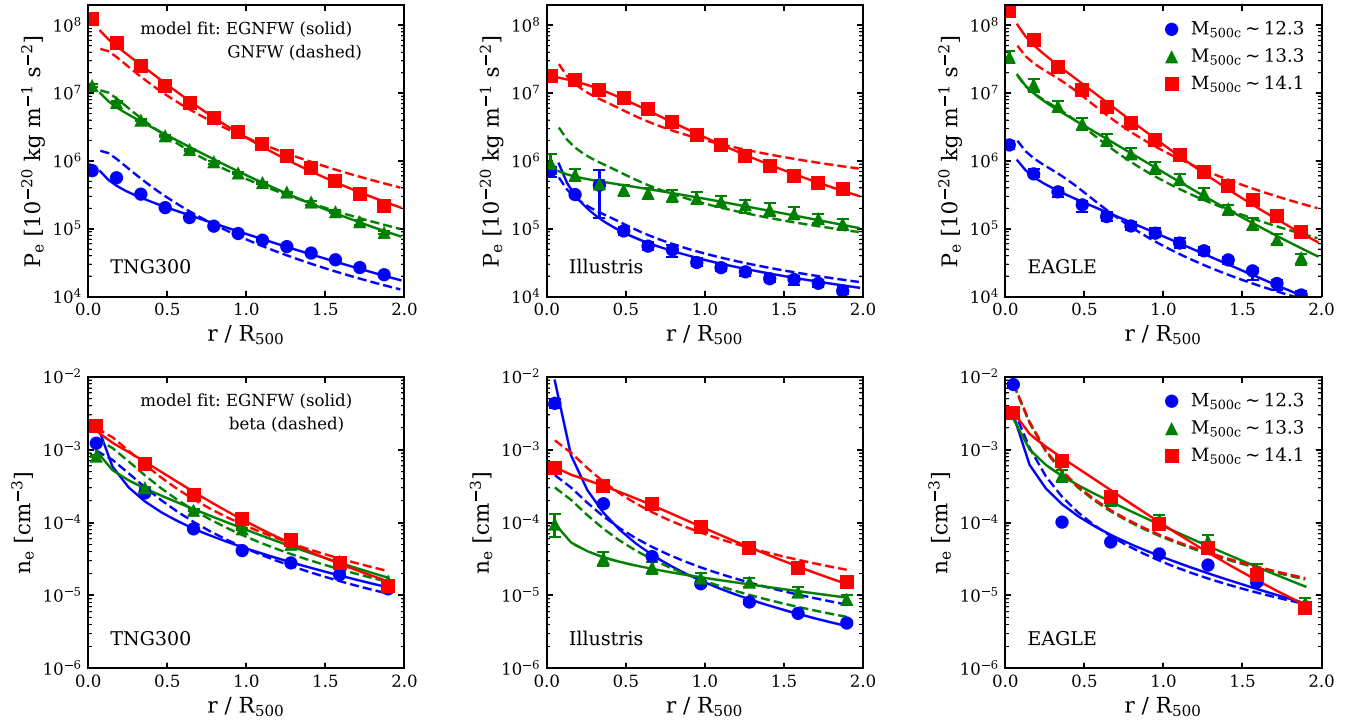
Figure 6. Profiles of halo gas from the simulations (symbols) with model fits (lines). For clarity, the results are shown only for three halo mass ranges as indicated in the right-hand panels. The error bars for the simulations indicate the 68 percentile ranges of the mean obtained from 10 000 bootstrap samples. Upper: The pressure profile fitted with the GNFW (dashed lines) and extended GNFW (EGNFW; solid lines) models. Lower: The electron density profile fitted with the β-profile (dashed lines) and EGNFW (solid lines) model.

the pressure distribution accurately, because the pressure profiles in haloes of different masses clearly have different shapes and thus are not matched only with normalizations. Specifically, it is seen, by comparing the dashed lines with the true profiles, that any mass-independent profiles including the GNFW would fail to match the profiles from the simulations because they overestimate at $r > 1.5\,R_{500}$ and at $r < 0.5\,R_{500}$ for massive and low-mass haloes, respectively. The positive δ's from our EGNFW model fit indicate that the pressure profile is less concentrated in lower mass haloes, consistent with the findings from previous studies such as LB15. This is because the gas is removed from the centre to the outer radii by feedback more effectively in the lower mass haloes due to their shallower potential well. Mass-independent profiles such as the GNFW, therefore, fail simply because they do not reflect the mass-dependent impact of feedback. The best-fitting parameter values are remarkably similar to what Gupta et al. (2017) reported for Magneticum, although the mass range explored is significantly different. The model fit to the profile predicted by EAGLE is shown to have higher values for both β and γ_0, which indicates steeper slopes both in the outer and inner regions of haloes, respectively, relative to

the other two simulations. The profiles directly measured from the simulations indeed show that EAGLE predicts steeper slopes at both the inner and outer radii.

We also fit the profile of electron number density with the β-profile and our EGNFW model. As seen in Fig. 6, the shape of the profile strongly depends on mass, thus cannot be well described by a mass-independent profile such as the β-profile. As can be seen, instead, our new EGNFW model describes well the density profiles with the best parameters as listed in Table 3. The negative ϵ's from our EGNFW model fit describe the steeper slope in the innermost region of lower mass haloes, which cannot be described well by the β-profile or the

Table 3. The best-fitting parameters of the EGNFW model for the density profile.

Profiles	β	γ_0	ϵ	$c_{500,0}$	δ
Illustris	4.03	0.203	-0.603	0.877	0.735
TNG300	3.50	0.288	-0.379	1.52	0.306
EAGLE	5.64	0.607	-0.219	0.979	0.261

EGNFW model from LB15. The concentration of the gas distribution is found to increase with increasing mass (i.e. positive δ's) as was the case for the pressure profiles.

4 SUMMARY AND DISCUSSION

In this paper, we have compared the gas properties of the circumgalactic (CGM) and intergalactic (IGM) media between an observational data set and a selection of cosmological simulations, to explore the possibility of using the gas content within and around haloes to test models for physics of galaxy evolution.

Specifically, we have used SZE results obtained following Lim et al. (2018a,b, 2020) as the observational data, and compared them with the predictions from four state-of-art cosmological hydrodynamical galaxy simulations at $z \sim 0$: Illustris, TNG300 of the IllustrisTNG project, EAGLE, and a Magneticum simulation run with a sidelength of $352\,h^{-1}$ Mpc. The observation data were obtained by cross-correlating *Planck* maps with haloes identified mainly in the SDSS data by a halo finder, and with reconstructed large-scale environments such as density field, tidal field, and velocity field.

For the tSZE signal from haloes (Fig. 1), the observational results and the predictions from all the simulations considered in this analysis indicate a certain degree of deviation from the self-similar case, indicating that feedback impacts strongly the gas content of haloes with $M_{500} \sim 10^{12-13}\,\mathrm{M_\odot}$. This is in contrast with the conclusions by the Planck Collaboration XI (2013, PCXI), who find that the tSZE flux follows the self-similar case down to low-mass haloes with $M_{500} \sim 10^{12}\,\mathrm{M_\odot}$. We suspect that the reason for such difference lies in the assumption of flat local background adopted by PCXI (Lim et al. 2018a). Different simulations make different tSZE signal predictions because of the different implementation of the underlying physical model. Illustris, in particular, predicts a significantly lower thermal energy of gas in haloes with $M_{500} \sim 10^{13-13.5}\,\mathrm{M_\odot}$. This is believed to be due to the stronger AGN feedback adopted in that simulation, consistently with the findings and discussions of previous studies (Genel et al. 2014; Pillepich et al. 2018a). The predictions for $\tilde{Y}_{500}$ from TNG300 and EAGLE are remarkably similar, down to $M_{500} \sim 10^{12}\,\mathrm{M_\odot}$.

The kSZE signal from the observational data (Fig. 2, left) implies that the gas fraction in haloes is almost equal to the cosmic baryon fraction even in $M_{500} \lesssim 10^{13}\,\mathrm{M_\odot}$ haloes, in contrast with the predictions from simulations where the baryon fraction in those haloes is only 20–40 per cent of the cosmic fraction. There can be still, however, the residual contamination by gas along the LOSs between haloes not taken into account. Such contamination is found to be about 20 per cent according to simulations (Lim et al. 2020) but is expected to depend too on the baryonic physics.

Similarly, the effective temperature from the observations (Fig. 2, right), obtained by dividing the tSZE flux with the kSZE flux, is also found to be up to one order of magnitude lower than that from the simulations. Notably, even the simulations with completely distinct feedback models produce very similar predictions, in that the halo gas is approximately at the virial temperature, whereas the prediction about the gas fraction varies much more significantly among the models. This indicates that the discrepancy between the predictions and the data may be due to other factors than the models implemented for feedback, such as the modelling of multiphase gas components.

Moving to the gas that surrounds haloes, we have investigated the pressure–density relation of the IGM (Fig. 3). The overall slope of the relation from both the observational data and the simulations closely follows that of an adiabatic equation of state. The observationally inferred relation matches well the predictions from the simulations,

except for Illustris that predicts a much higher thermal energy of IGM in the regions of intermediate density, this being too a manifestation of the strongly ejective AGN feedback at low accretion rates adopted in Illustris.

However, the dependence of the pressure–density relation on the tidal field strength (Fig. 4) is shown to have an important testing power for the models: All simulations fail to match the dependence for underdense regions inferred from the observation in detail. On the other hand, the prediction by TNG300 matches the observation significantly better than EAGLE for the regions with an intermediate density of $(1$–$10)\,\overline{\rho}_{\mathrm{m}}$, which corresponds to cosmic structures such as filaments. We speculate that this may be because TNG300 employs two different modes to model AGN feedback, unlike the single-mode thermal model in EAGLE, and the 'wind-mode' feedback – which in TNG300 has been shown to be more effective than the thermal mode at displacing gas (e.g. Zinger et al. 2020) – is more active in the regions with a stronger tidal field. Also, the mismatch of the TNG300 prediction with the observation for the underdense region indicates an interesting hint that the current balance between the different modes of AGN feedback could potentially be adjusted to alleviate the tension. Specifically, the much stronger dependence on the tidal field strength found from the observation requires feedback mechanism(s) with clearly distinct strengths/modes in regions of different tidal fields in voids or underdense part of the Universe. This might be achieved by fine-tuning the model parameters that control the feedback efficiency, i.e. breaking potentially remaining degeneracy in the parameter constraints by other observations. Although it is beyond the scope of this paper, this could be explored in future work with simulations where the observations presented in this paper are used to constrain the physical parameters jointly together with other observations previously used as the empirical constraints for simulations. All this shows that the tidal field dependence of the IGM gas property can provide a significantly more stringent test to break the degeneracy between models that produce similar predictions otherwise.

Finally, we have probed the profiles of gas properties in haloes predicted from the simulations (Figs 5 and 6). Different simulations predict differently shallow profiles of gas pressure and temperature, with more or less gas near the halo centre, depending on the efficiency of the differently implemented AGN feedback models at displacing gas. The most prominent differences across models occur in intermediate-mass haloes with $M_{500} \sim 10^{13-13.5}\,\mathrm{M_\odot}$, which are hence a promising target to test AGN feedback.

The profiles from the simulations are not well described by a GNFW profile or β-profile, both of which describe profiles with a universal shape regardless of mass unlike the profiles measured from the simulations. We demonstrate that a mass-dependent model is required to describe the simulated profiles accurately. Specifically, our new model (EGNFW), which incorporates such mass dependence in the innermost slope and concentration of the profiles, is shown to describe both the pressure and density profiles accurately out to $2R_{500}$.

Our study clearly demonstrates the power of using the SZE to test galaxy formation models. In particular, because most state-of-art simulations have their model parameters chosen to match a range of average properties of observed galaxies (in their stellar components, in particular), it is essential to take into account correlations in the properties of their gas, host haloes, and large-scale environment, in order to break the degeneracy among models. The haloes with mass between 10^{12} and $10^{14.5}$ studied in this paper are effectively impacted by AGN feedback and therefore offer a strong testing power for theory. With future CMB surveys such as the CMB-S4 (Abazajian

et al. 2016, 2019; Abitbol et al. 2017), Simons Observatory (Galitzki 2018a; Galitzki et al. 2018b; Ade et al. 2019), and Toltec (Bryan et al. 2018), it is also expected that the SZE will allow us to probe the gas profiles of low-mass systems down to $M_{500} \sim 10^{12}\,M_\odot$ by stacking (see also Battaglia et al. 2017, 2019). Similar comparisons as explored in this study can be applied to the future surveys to provide stringent tests on theoretical models of galaxy formation.

ACKNOWLEDGEMENTS

DATA AVAILABILITY

The data underlying this article will be shared on reasonable request to the corresponding author.

REFERENCES

Abazajian K. N. et al., 2009, ApJS, 182, 543
Abazajian K. N. et al., 2016, preprint (arXiv:1610.02743)
Abazajian K. N. et al., 2019, preprint (arXiv:1907.04473)
Abitbol M. H. et al., 2017, preprint (arXiv:1706.02464)
Ade P. et al., 2019, JCAP, 02, 056
Anglés-Alcázar D., Faucher-Giguère C.-A., Kereš D., Hopkins P. F., Quataert E., Murray N., 2017, MNRAS, 470, 4698
Arnaud M., Pratt G. W., Piffaretti R., Böhringer H., Croston J. H., Pointe-couteau E., 2010, A&A, 517, 92
Ayromlou M., Nelson D., Yates R. M., Kauffmann G., Renneby M., White S. D. M., 2020, MNRAS, 502, 1051
Barnes D. J. et al., 2017, MNRAS, 471, 1088
Battaglia N., Bond J. R., Pfrommer C., Sievers J. L., 2012, ApJ, 758, 74
Battaglia N., Bond J. R., Pfrommer C., Sievers J. L., 2012, ApJ, 758, 75
Battaglia N., Ferraro S., Schaan E., Spergel D. N., 2017, JCAP, 2017, 040
Battaglia N. et al., 2019, BAAS, 51, 297
Biffi V., Dolag K., Böhringer H., 2013, MNRAS, 428, 1395
Booth C. M., Schaye J., 2009, MNRAS, 398, 53
Borthakur J. K. et al., 2016, ApJ, 833, 259
Bryan S. et al., 2018, in Jonas Z., Jian-Rong G., eds, Proc. SPIE Conf. Ser. Vol. 10708, Millimeter, Submillimeter, and Far-Infrared Detectors and Instrumentation for Astronomy IX. SPIE, Bellingham. p. 107080J
Chabrier G., 2003, PASP, 115, 763
Chisholm J., Tremonti C. A., Leitherer C., Chen Y., Wofford A., 2016, MNRAS, 457, 3133
Crain R. A. et al., 2015, MNRAS, 450, 1937
Davis M., Efstathiou G., Frenk C. S., White S. D. M., 1985, ApJ, 292, 371
de Graaff A., Cai Y.-C., Heymans C., Peacock J. A., 2019, A&A, 624, 48
Dolag K., Jubelgas M., Springel V., Borgani S., Rasia E., 2004, ApJ, 606, 97
Dolag K., Komatsu E., Sunyaev R., 2016, MNRAS, 463, 1797
Fabjan D., Borgani S., Tornatore L., Saro A., Murante G., Dolag K., 2010, MNRAS, 401, 1670
Fattahi A. et al., 2016, MNRAS, 457, 844
Faucher-Giguère C.-A., Kereš D., Dijkstra M., Hernquist L., Zaldarriaga M., 2010, ApJ, 725, 633
Faucher-Giguère C.-A., Kereš D., Ma C. P., 2011a, MNRAS, 417, 2982
Faucher-Giguère C.-A., Kereš D., 2011b, MNRAS, 412, 118
Faucher-Giguère C.-A., Hopkins P. F., Kereš D., Muratov A. L., Quataert E., Murray N., 2015, MNRAS, 449, 987
Faucher-Giguère C.-A., Feldmann R., Quataert E., Kereš D., Hopkins P. F., Murray N., 2016, MNRAS, 461, L32
Galitzki N., 2018a, preprint (arXiv:1810.02465)
Galitzki N. et al., 2018b, in Jonas Z., Jian-Rong G., eds, Proc. SPIE Conf. Ser. Vol. 10708, Millimeter, Submillimeter, and Far-Infrared Detectors and Instrumentation for Astronomy IX. SPIE, Bellingham, p. 1070804
Genel S. et al., 2014, MNRAS, 445, 175
Genel S., Fall S. M., Hernquist L., Vogelsberger M., Snyder G. F., Rodriguez-Gomez V., Sijacki D., Springel V., 2015, ApJ, 804, 40
Giodini S. et al., 2009, ApJ, 703, 982
Gonzalez A. H., Sivanandam S., Zabludoff A. I., Zaritsky D., 2013, ApJ, 778, 14
Grand R. J. J. et al., 2017, MNRAS, 467, 179
Gupta N., Saro A., Mohr J. J., Dolag K., Liu J., 2017, MNRAS, 469, 3069
Hafen Z. et al., 2019, MNRAS, 488, 1248
Hand N. et al., 2012, Phys. Rev. Lett., 109, 041101
Heckman T. M., Alexandroff R. M., Borthakur S., Overzier R., Leitherer C., 2015, ApJ, 809, 147
Hernández-Monteagudo C., Ma Y.-Z., Kitaura F. S., Wang W., Génova-Santos R., Macías-Pérez J., Herranz D., 2015, Phys. Rev. Lett., 115, 191301
Hill J. C., Ferraro S., Battaglia N., Liu J., Spergel D. N., 2016, Phys. Rev. Lett., 117, 051301
Hill J. C., Baxter E. J., Lidz A., Greco J. P., Jain B., 2018, Phys. Rev. D, 97, 083501
Hinshaw G. et al., 2013, ApJS, 208, 19
Hirschmann M., Dolag K., Saro A., Bachmann L., Borgani S., Burkert A., 2014, MNRAS, 442, 2304
Hojjati A., McCarthy I. G., Harnois-Deraps J., Ma Y.-Z., Van Waerbeke L., Hinshaw G., Le Brun A. M. C., 2015, JCAP, 10, 047
Hopkins P. F., Kereš D., Onorbe J., Faucher-Giguère C.-A., Quataert E., Murray N., Bullock J. S., 2014, MNRAS, 445, 581
Hopkins P. F. et al., 2018, MNRAS, 480, 800
Huchra J. P., Geller M. J., 1982, ApJ, 257, 423
Hummels C. B., Bryan G. L., Smith B. D., Turk M. J., 2013, MNRAS, 430, 1548
Jones T., Stark D. P., Ellis R. S., 2012, ApJ, 751, 51
Katz N., Weinberg D. H., Hernquist L., 1996, ApJS, 105, 19
Kereš D., Katz N., Weinberg D. H., Davé R., 2005, MNRAS, 363, 2
Kereš D., Katz N., Fardal M., Davé R., Weinberg D. H., 2009, MNRAS, 395, 160
Komatsu E. et al., 2011, ApJS, 192, 18
Le Brun A. M. C., McCarthy I. G., Melin J.-B., 2015, MNRAS, 451, 3868 (LB15)
Lee E., Chluba J., Kay S. T., Barnes D. J., 2020, MNRAS, 493, 3274
Lim S. H., Mo H. J., Lu Y., Wang H., Yang X., 2017, MNRAS, 470, 2982
Lim S. H., Mo H. J., Li R., Liu Y., Ma Y.-Z., Wang H., Yang X., 2018a, ApJ, 854, 181 (L18a)
Lim S. H., Mo H. J., Wang H., Yang X., 2018b, ApJ, 480, 4017 (L18b)
Lim S. H., Mo H. J., Wang H., Yang X., 2020, ApJ, 889, 48 (L20)
Lovisari L., Reiprich T. H., Schellenberger G., 2015, A&A, 573, 118

Ma Y.-Z., Van Waerbeke L., Hinshaw G., Hojjati A., Scott D., Zuntz J., 2015, JCAP, 9, 046

McAlpine S. et al., 2016, Astron. Comput., 15, 72

McCarthy I. G., Schaye J., Bird S., Le Brun A. M. C., 2017, MNRAS, 465, 2936

Marinacci F. et al., 2018, MNRAS, 480, 5113

Martin C. L. et al., 2012, ApJ, 760, 127

Mo H. J., van den Bosch F. C., White S. D. M., 2010, Galaxy Formation and Evolution. Cambridge Univ. Press, New York, NY

Muratov A. L., Kereš D., Faucher-Giguère C.-A., Hopkins P. F., Quataert E., Murray N., 2015, MNRAS, 454, 2691

Nagai D., Vikhlinin A., Kravtsov A. V., 2007a, ApJ, 655, 98

Nagai D., Kravtsov A. V., Vikhlinin A., 2007b, ApJ, 668, 1

Naiman J. P. et al., 2018, MNRAS, 477, 1206

Nelson D. et al., 2018, MNRAS, 475, 624

Nelson D. et al., 2018, MNRAS, 477, 450

Newman S. F. et al., 2012, ApJ, 761, 43

Oppenheimer B. D., 2018, MNRAS, 480, 2963

Oppenheimer B. D. et al., 2020, ApJ, 893, L24

Pakmor R., Hachinger S., Röopke F. K., Hillebrandt W., 2011, A&A, 528, 117

Pillepich A. et al., 2018a, MNRAS, 473, 4077

Pillepich A. et al., 2018b, MNRAS, 475, 648

Plagge T. et al., 2010, ApJ, 716, 1118

Planck Collaboration I, 2011, A&A, 536, 1

Planck Collaboration XI, 2013, A&A, 557, 52 (PCXI)

Planck Collaboration XIII, 2016, A&A, 594, 13

Planck Collaboration XVI, 2014, A&A, 571, 16

Prochaska J. X. et al., 2017, ApJ, 837, 169

Remazeilles M., Bolliet B., Rotti A., Chluba J., 2019, MNRAS, 483, 3459

Rosas-Guevara Y. M. et al., 2016, MNRAS, 462, 190

Rubin K. H. R. et al., 2014, ApJ, 794, 156

Rudie G. C., Steidel C. C., Pettini M., Trainor R. F., Strom A. L., Hummels C. B., Reddy N. A., Shapley A. E., 2019, ApJ, 885, 61

Sawala T. et al., 2016, MNRAS, 457, 1931

Schaye J., Dalla Vecchia C., 2008, MNRAS, 383, 1210

Schaye J. et al., 2015, MNRAS, 446, 521

Sijacki D., Springel V., Di Matteo T., Hernquist L., 2007, MNRAS, 380, 877

Sijacki D., Vogelsberger M., Genel S., Springel V., Torrey P., Snyder G. F., Nelson D., Hernquist L., 2015, MNRAS, 452, 575

Somerville R. S., Davé R., 2015, ARA&A, 53, 51

Springel V., 2005, MNRAS, 364, 1105

Springel V., 2010, MNRAS, 401, 791

Springel V., Hernquist L., 2003, MNRAS, 339, 289

Springel V. et al., 2005, Nature, 435, 629

Springel V. et al., 2018, MNRAS, 475, 676

Steidel C. C., Erb D. K., Shapley A. E., Pettini M., Reddy N., Bogosavljević M., Rudie G. C., Rakic O., 2010, ApJ, 717, 289

Stocke J. T. et al., 2013, ApJ, 763, 148

Sun M., Voit G. M., Donahue M., Jones C., Forman W., Vikhlinin A., 2009, ApJ, 693, 1142

Sunyaev R. A., Zeldovich Y. B., 1972, Comments Astrophys. Space Phys., 4, 173

Tanimura H., Hinshaw G., McCarthy I. G., Van Waerbeke L., Ma Y.-Z., Mead A., Hojjati A., Tröster T., 2019, MNRAS, 483, 223

Tauber J. A. et al., 2010, A&A, 520, 1

Torrey P., Vogelsberger M., Genel S., Sijacki D., Springel V., Hernquist L., 2014, MNRAS, 438, 1985

Truong N. et al., 2020, MNRAS, 494, 549

Tumlinson J., Peeples M. S., Werk J. K., 2017, ARA&A, 55, 389

van de Voort F. et al., 2016, MNRAS, 463, 4533

Van Waerbeke L., Hinshaw G., Murray N., 2014, Phys. Rev. D, 89, 023508

Vikhlinin A., Kravtsov A., Forman W., Jones C., Markevitch M., Murray S. S., Van Speybroeck L., 2006, ApJ, 640, 691

Vikram V., Lidz A., Jain B., 2017, MNRAS, 467, 2315

Vogelsberger M., Genel S., Sijacki D., Torrey P., Springel V., Hernquist L., 2013, MNRAS, 436, 3031

Vogelsberger M. et al., 2014a, MNRAS, 444, 1518

Vogelsberger M. et al., 2014b, Nature, 509, 177

Wang H., Mo H. J., Jing Y. P., Yang X., Wang Y., 2011, MNRAS, 413, 1973

Wang H., Mo H. J., Yang X., van den Bosch F. C., 2012, MNRAS, 420, 1809

Wang H. et al., 2016, ApJ, 831, 164

Weinberger R. et al., 2017, MNRAS, 465, 3291

Werk J. K. et al., 2014, ApJ, 792, 8

Werk J. K. et al., 2016, ApJ, 833, 54

Wiersma R. P. C., Schaye J., Smith B. D., 2009a, MNRAS, 393, 99

Wu X., Mo H., Li C., Lim S., 2020, ApJ, 903, 26

Yang X., Mo H. J., van den Bosch F. C., Jing Y. P., 2005, MNRAS, 356, 1293

Yang X., Mo H. J., van den Bosch F. C., Pasquali A., Li C., Barden M., 2007, ApJ, 671, 153

Zinger E. et al., 2020, MNRAS, 499, 768

This paper has been typeset from a TEX/LATEX file prepared by the author.